Scanning Microscopy

Volume 1993
Number 7 *Physics of Generation and Detection of Signals Used for Microcharacterization*

Article 15

1993

X-Ray Topography

A. Zarka
Laboratoire de Minéralogie-Cristallographie de Paris, France

Scanning Microscopy Supplement 7, 1993 (Pages 221-242)
Scanning Microscopy International, Chicago (AMF O'Hare), IL 60666 USA

0892-953X/93$5.00+.25

X-RAY TOPOGRAPHY

A. Zarka

Laboratoire de Minéralogie-Cristallographie de Paris
4 Place Jussieu, 75252, Paris Cedex 05, France
Phone No.: (1) 44 27 52 25; Fax No.: (1) 44 27 37 85

Abstract

The purpose of this paper is to discuss some elements of dynamical theory and to introduce some basic ideas on defect image formation in X-ray topographs. After some explanations of the basic principles of dynamical theory of X-rays, examples of defect contrast are given. Two examples of studies of quartz single crystals by X-ray topography are developed. First, the analysis of the X-ray spherical wave topographs of various Y-cut plates of synthetic quartz crystals show that the coherence of the lattice between the seed and the grown crystal is directly related to the density of the dislocations present in the seed. For the samples, the local deformations are essentially related to the density of the dislocations. Plane-wave topography shows that the local deformations can be estimated with good precision and related to the growth defects. The second example concerns Stroboscopic X-ray topography. With the use of synchrotron radiation, we have examined three quartz resonators. Several types of vibration modes and the perturbations due to the defects are described. Defects such as growth bands and especially dislocations disturb acoustic wave propagation in the crystals and can induce losses by untrapping a part of the energy of the mode conversion.

Key Words: X-ray topography, quartz, stroboscopy, synchrotron radiation, growth defects.

Introduction

The topographic technique for studying imperfection in nearly perfect crystals was developed 30 years ago by Lang [11] among others. It is now widely used throughout the world and has received many applications. Its principle is based mainly on the difference in the intensities of X-rays diffracted by deformed and perfect regions of the crystal [5, 14, 25].

The aim of this paper is to first give the theoretical basis necessary for the interpretation of the contrast of the images of the defects on X-ray topographs and then show examples of possible studies. The first part of the paper is devoted to the theory of the diffraction of X-rays by a perfect crystal, the second part to the principles of various topographic techniques and the third part to applications through the study of quartz crystals.

Dynamical Theory of the Diffraction

Two main theories have been developed to interpret the intensities of X-rays diffracted by a crystal: the geometric or kinematical theory and the dynamical theory.

Kinematical theory

In the kinematical theory, it is assumed that the amplitudes of X-rays incident on all diffracted centers of the crystal are the same. This leads to a very simplified calculation of the global intensity diffracted by the crystal which is only valid for very thin crystals or, more generally, very imperfect crystals.

Studying the diffraction by a thick perfect crystal, one has to take into account all the interactions between the incident and diffracted waves. It can be shown that for very thin crystals or highly deformed crystals the results of the dynamical theory tend asymptotically towards those of the kinematical theory.

Dynamical theory

Diffraction by a perfect crystal. Let us consider a plane parallel slab and a transmission setting. In order for the dynamical theory to apply, we must assume that the specimen thickness is not too small (otherwise, the kinematic theory could be used).

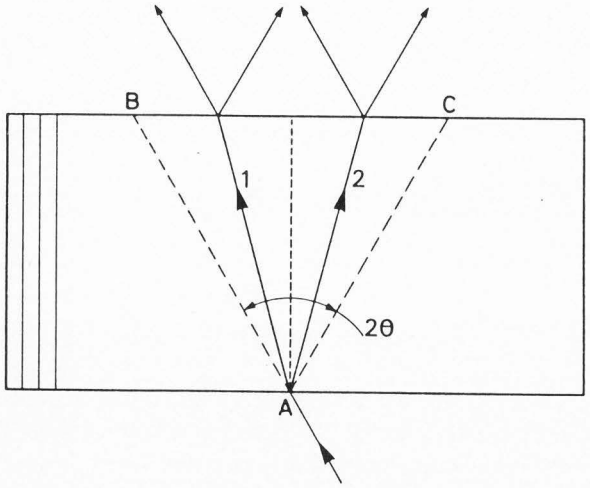

Figure 1. Diffraction of a plane wave (Direct Space).

Plane wave case. Following Laue's treatment, we shall look for those solutions of Maxwell's equations which are compatible with the triperiodicity of the medium. A plane wave, characterized by its wave vector $\vec{k}$, far from the diffraction conditions, gives rise in the crystal to a transmitted (refracted) wave with wave vector $\vec{k}_o = n\vec{k}$, where n is the index of refraction. The diffraction condition can then be stated as:

$$\vec{k}_h = \vec{k}_o + \vec{h} \tag{1}$$

where $\vec{h}$ is a reciprocal lattice vector.

A solution to the propagation equation can easily be obtained in the form of a Bloch wave. In the two beam case, such a Bloch wave is the superposition of two plane waves:

$$\vec{D} = \vec{D}_o\, e^{-2\Pi i \vec{K}_o \cdot \vec{r}} + \vec{D}_h\, e^{-2\Pi i \vec{K}_h \cdot \vec{r}} . \tag{2}$$

This superposition is called a wavefield, a concept which is very useful when one wishes to understand the physics of the propagation of an X-ray wave.

If the incident wave is a pseudo plane wave (i.e., a "plane" wave of finite lateral extension), two wavefields propagate inside the crystal (Figure 1). The direction of these wavefields depends on the departure of the incident wave from the exact Bragg angle (as it is given by Bragg's formula).

Wavefield propagation inside the crystal can easily be handled by consideration of the reciprocal space. Two spheres of radius k centered at O and H (two lattice points of the reciprocal space) are drawn; in the plane of incidence, these two spheres give two circles intersecting at point L_a (Figure 2a), the center of Ewald's sphere. Two other spheres of radius K_o, also centered at O and H are drawn. Diffraction occurs when the extremity of $\vec{k}_o$ lies near L_a. The extremities of those wave-vectors which correspond to propagation inside the crystal lie on a surface which is called the dispersion surface. Close to the diffraction conditions, the intersection of this surface with the plane of incidence is no longer made of two circles intersecting at L_a; it is split into two branches of a hyperbola as shown in Figure 2b. The two branches of the hyperbola which asymptotically merge in the two circles are separated by a distance which is about 10^6 times smaller than the radius of those circles; so that in the vicinity of L_a these circles can be approximated by their two asymptotes T_o and T_h (Figure 2c).

In fact, due to the electromagnetic nature of X-rays, polarization should be taken into account in the description of the X-ray wave; this gives rise to two hyperbolae π and σ (one for each eigenstate of polarization) rather than one. S_1S_2, the diameter of a given hyperbola is then, for a symmetric reflection,

$$\frac{|C|\sqrt{\chi_h \chi_{\bar{h}}}}{\cos\Theta}, \tag{3}$$

where $|C| = 1$ or $\cos 2\Theta$ depending on the polarization, χ_h and $\chi_{\bar{h}}$ are the h and $\bar{h}$ coefficients of the Fourier expansion of the electric susceptibility χ.

The incident wave is represented by a point M lying on the circle of radius k, so that

$$\Delta\Theta = \frac{\overline{L_aM}}{k}, \tag{4}$$

where $\Delta\Theta$ is the departure from the exact Bragg's angle. A convenient parameter is:

$$\eta = \frac{\Delta\Theta \sin 2\Theta}{|C|(\chi_o \chi_{\bar{h}})^{1/2}}. \tag{5}$$

The normal to the crystal faces drawn from M then intersects the dispersion surface at P_1 and P_2 which are the characteristic points of the wavefields which propagate inside the crystal. Since the location of P_1 and P_2 depend on η, the directions of propagation of the two wavefields (which are normal to the dispersion surface at P_1 and P_2, respectively), also depend on the departure from the exact Bragg's angle.

To each direction or propagation inside the crystal there correspond two coherent waves, the spatial periodicity of which is

$$\Lambda = \frac{\Lambda_0}{\sqrt{1 + \eta_r^2}}, \tag{6}$$

Λ_0 being the inverse of the diameter S_1S_2; η_r here is the

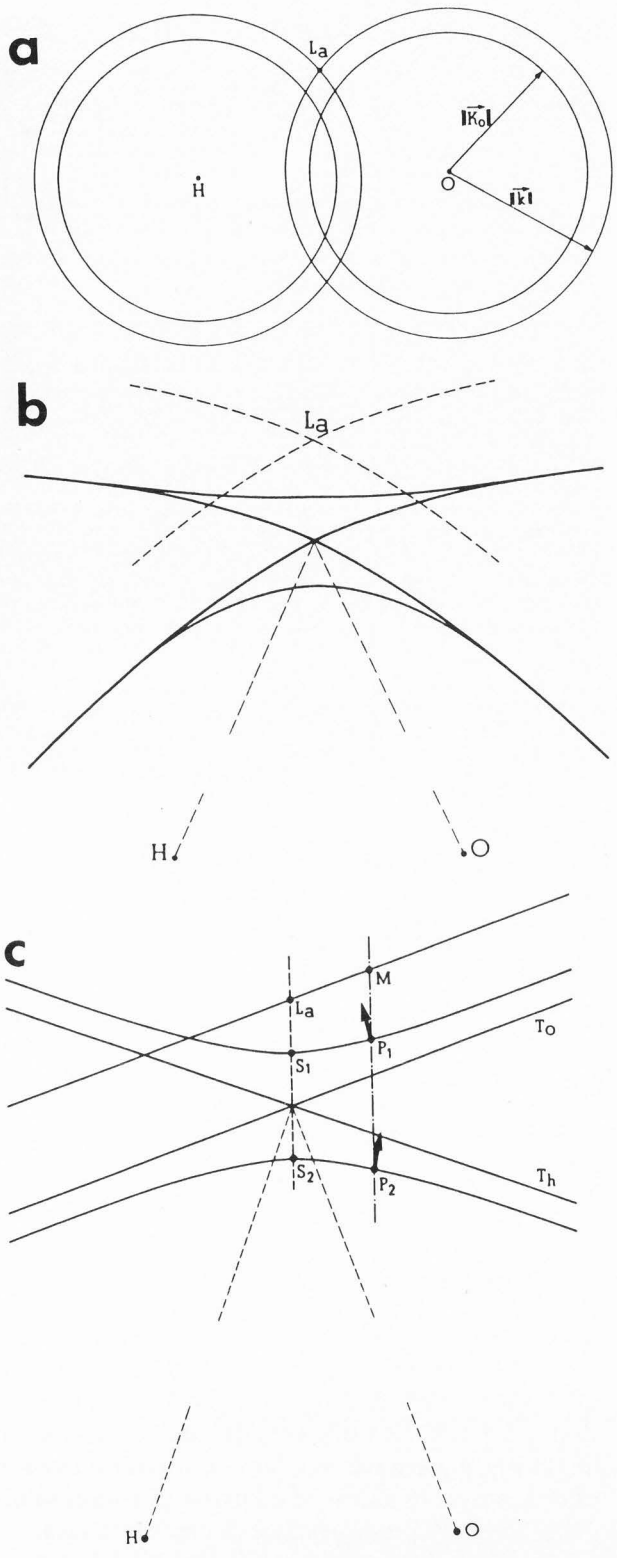

Figure 2. (**a**) Spheres centered at the reciprocal lattice point O and H showing the position of the Laue point L_a. (**b**) Dispersion surface. (**c**) Dispersion surface: close-up view.

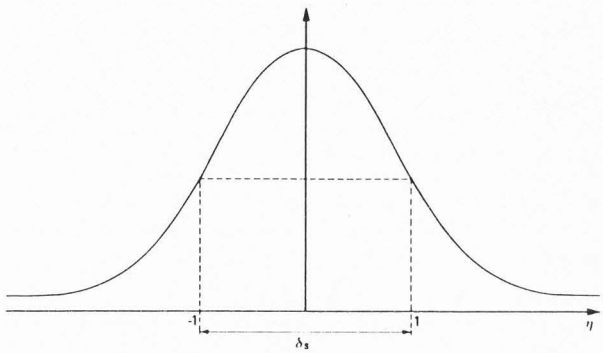

Figure 3. Perfect crystal. Reflecting curve.

real part of η. This phenomenon is called Pendellösung, after Ewald. Λ is usually called the Pendellösung wavelength, or extinction distance; Λ_0 is the Pendellösung wavelength inside the reflecting plane.

Intrinsic rocking curve. For a symmetric reflection, the full width at half maximum (FWHM) is approximately (see Figure 3) :

$$\delta_S = \frac{2R}{V} \lambda^2 \frac{F_h}{\sin 2\theta_B}, \qquad (7)$$

where R is the so-called classical radius of the electron, λ the radiation wave-length, V the volume of the unit cell and F_h the structure factor. Expression (4) holds for both transmission and reflection settings. Typical values of FWHM are of the order of a few arc seconds. This parameter was first introduced as a measure of the crystal perfectness. This is achieved by means of a double crystal setting (+,-), using two parallel and identical crystals for the same reflection [3]; the experimental FWHM of the second crystal is then obtained from the convolution of the two individual FWHM, i.e., $\delta\sqrt{2}$ in the case of two perfect crystals.

This technique is now being used when studying epitaxial layers as in heterojunctions of III-V compounds, garnets and so on. The best experimental results are obtained by using a plane wave as means of exploration of the crystal to be studied. This technique was initiated by the those working with Kohra [10] in Japan who designed and realized the first multiple reflection monochromators. Plane waves of reasonable intensity can be fairly easily obtained by using synchrotron radiation [15].

The concept of FWHM is of importance in topographic techniques since it gives a qualitative estimation of the width of the so-called direct dislocation images.

Spherical wave. X-ray tubes deliver waves which must be described as spherical waves. In most experimental set-ups, the divergence of the X-ray beam

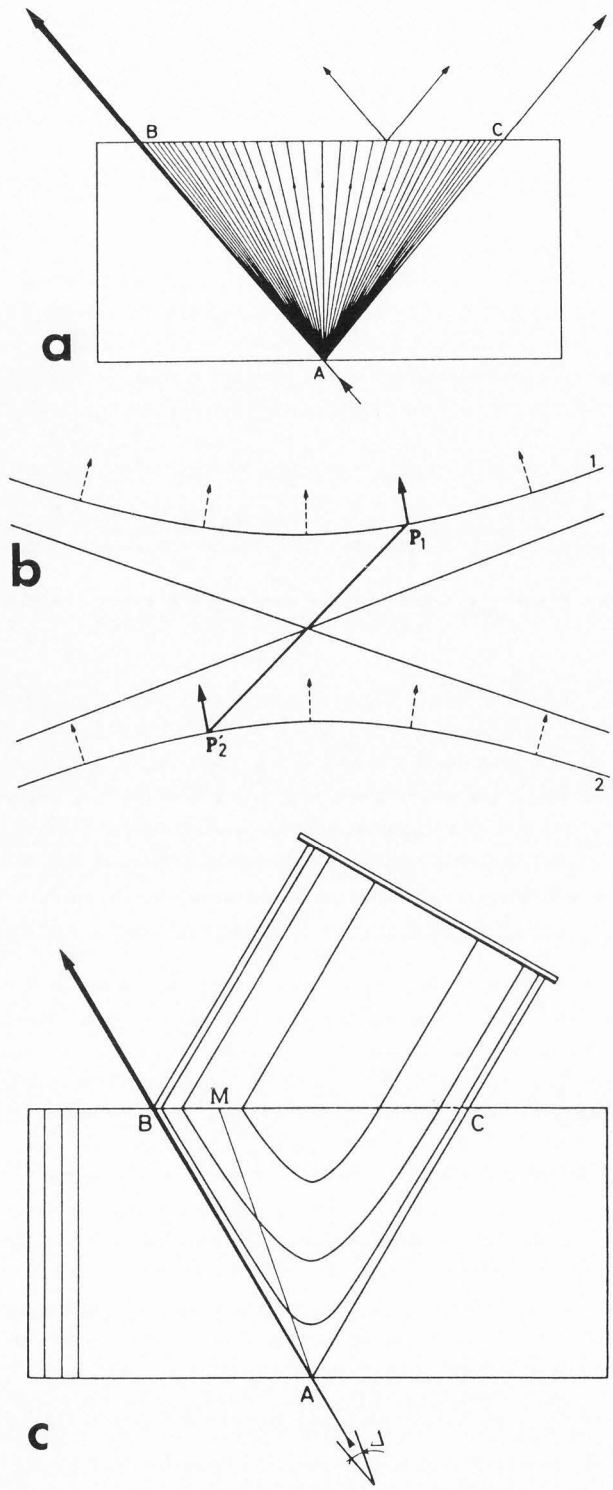

Figure 4. (**a**) Diffraction of a spherical wave: fanning out of the wave-fields. (**b**) Dispersion surface. (**c**) Interference maxima. (**d**) Section topograph. (**e**) Principle of section topography.

incident on the crystal is therefore much larger than the width of the rocking curve, and the Laue plane wave theory cannot be applied. Various theoretical treatments [7, 8, 9] have been developed in order to deal with non-plane waves. We shall be concerned here with one of them, namely Kato's treatment of spherical waves. In this theory, a given spherical wave is expanded as a sum of plane waves by means of a Fourier transform so that the notion of dispersion surface can be maintained.

Let us assume an incident beam having a divergence Δ, such that

$$\Delta \gg \delta. \tag{8}$$

The whole dispersion surface is then excited and the X-ray beam intensity is distributed inside a fan of angle

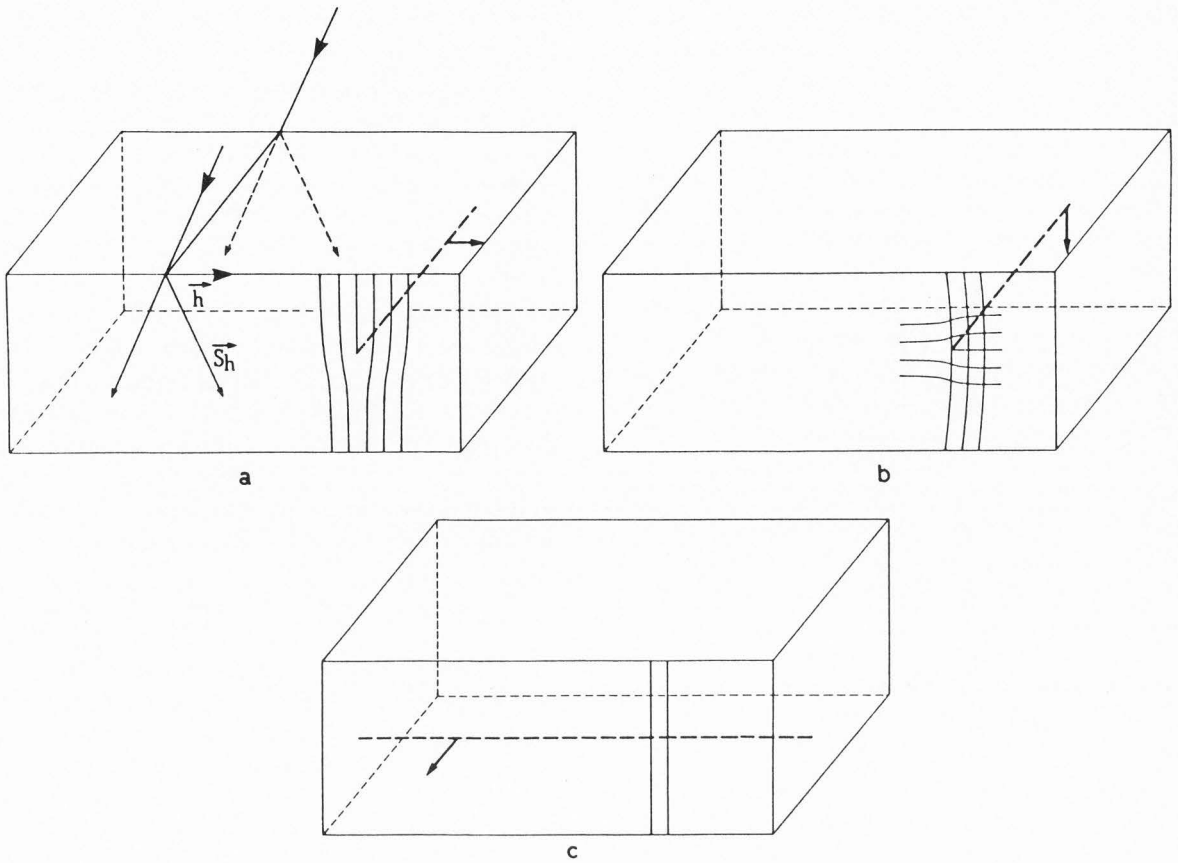

Figure 5. Schematic explanation of the diffracting planes deformation for a pure edge dislocation.

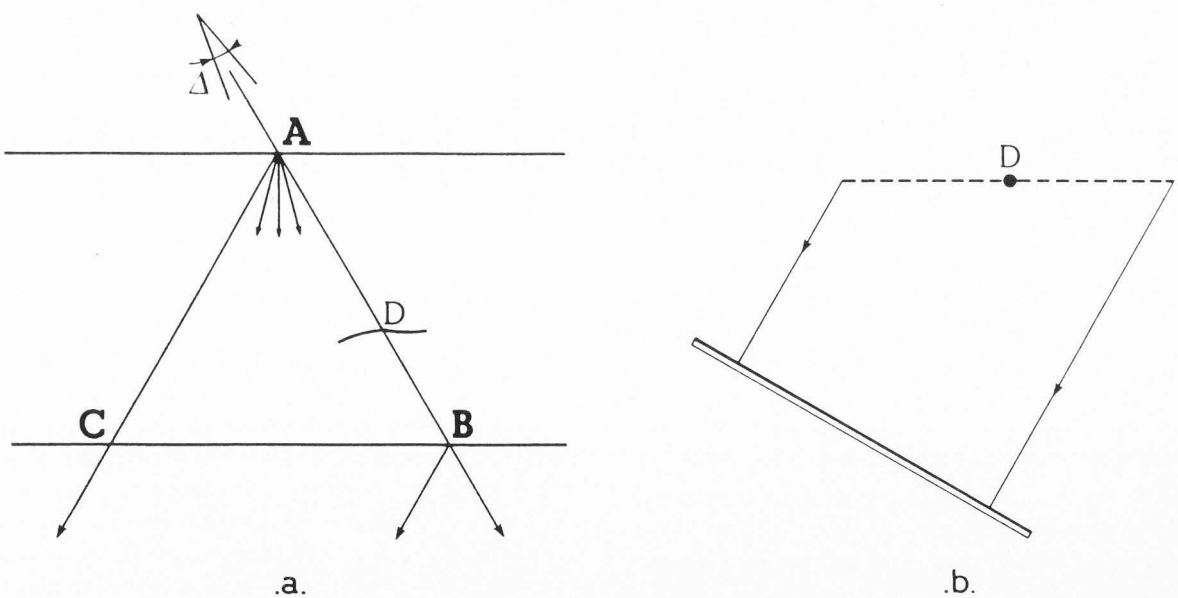

Figure 6. (**a**) The dislocation cuts the direct beam in D. (**b**) The misoriented regions around D give rise to the direct image.

2Θ, lying between the incident and the reflected directions (see Figure 4a). Therefore, although the divergence of the useful part of the incident beam is only a few arc seconds, the divergence of the corresponding wavefields inside the crystal is of the order of several degrees. In other words, a large angular amplification is to be observed. Another important feature of the propagation in the spherical wave case is the following: the two wavefields which propagate along a given path, AM, inside the crystal correspond to two conjugate points P_1 and P'_2 on the hyperbolic dispersion surface (see Figures 4b and 4c). Two wavefields like these which are excited by the same incident wave and propagate along the same trajectory must interfere; Kato has shown that the corresponding maxima of these interferences are distributed on hyperbolae, the asymptotes of which lie along the incident and reflected directions. The distance between two successive maxima as measured along the axis of these hyperbolae is just Λ_0, the Pendellösung wavelength introduced in the case of an incident plane wave.

A photographic plate in the reflected beam will then show a set of parallel lines, the existence of which can be considered as an indication of the crystal perfection (Figure 4d).

In the case of weak absorption, a high density of wavefields is to be observed along AB and AC (Figure 4c), resulting in a margin effect (Figure 4d). The topograph shown on Figure 4d was obtained using the Lang technique (Figure 4e). For absorbing materials, wavefield 2 is strongly absorbed; the intensity on the exit surface is therefore mainly due to wavefield 1; in this case, no fringes are observed.

A simultaneous translation of the crystal and the photographic plate (traverse topography) will then give rise (assuming a perfect and parallel slab) to a uniform contrast on the photographic plate.

Diffraction by a non-perfect crystal. In order to treat the case of a distorted crystal (neither perfect nor mosaic), two different approaches are possible: one can develop either a global theory or a ray theory.

Global theory (Takagi [20], Taupin [22]). In this theory, the amplitude of the crystal wave at a given point is calculated. The concepts of dispersion surface and of wavefields cannot be maintained which can be viewed as the main drawback of this kind of approach since these notions are very useful if one wishes to visualize the diffraction process. Takagi and Taupin equations (partial differential equations), in principle, contain all the information concerning the wave in the crystal whatever its local deformations may be. Nevertheless, these equations can be solved analytically only in a limited number of cases. The general case can be treated using a computer. The importance of Takagi-Taupin's theory, therefore, comes from its ability to deal with any kind of defect.

Ray theory (Penning and Polder [18], Kato [6]). In these theories, it is assumed that it is possible to define a local dispersion surface in each region of the distorted crystal. This is valid only as long as the crystal deformations do not vary too rapidly. By analogy with the theory of light propagation in a medium of slowly varying index of refraction, a theory of wavefield propagation is then developed. It is clear that, in the case of a crystal containing a dislocation, for example, these theories cannot be applied in the regions right to the core of the dislocation. This prevents one from using such theories in order to perform computer simulations of a dislocation image. But, contrary to the global theory, this theory provides useful qualitative information concerning the diffraction process.

Defect Imaging and Characterization

Among all kinds of possible crystal defects, only a relatively small number can be visualized using topographic techniques. These can be classified as such:

- linear defects (dislocation);
- two-dimensional defects (subgrain boundaries, twin boundaries, stacking faults, antiphase-boundaries, domain walls in magnetic or ferroelectric materials, growth sector boundaries, growth bands,...); and
- inclusions, precipitates, swirls,...

Defects such as dislocations or stacking faults are defects which can be unambiguously characterized by a vector, be it the vector $\vec{b}$ in one case or the fault vector $\vec{f}$ in the other. These defects are easily imaged on topographs, and their characteristic parameters can, in principle, be determined. Other defects are not so easy to characterize, either because their structure is not completely known (which is the case for domain walls in ferroelectrics) or because they cannot be assigned quantitative definition (which is the case of growth bands which nevertheless are extensively studied).

Another requisite, if one wishes to characterize a defect, is that the defect should be isolated or at least that the density of such defects be low enough: this last restriction comes from the lack of resolving power of the topographic technique, as compared to transmission electron microscopy. One therefore must always first find the most adequate technique among those available and even use several techniques, as for example, in the case of the Lang technique, combining traverse and section topography.

Local variations of the departure from Bragg's law

The effective misorientation, or local departure from

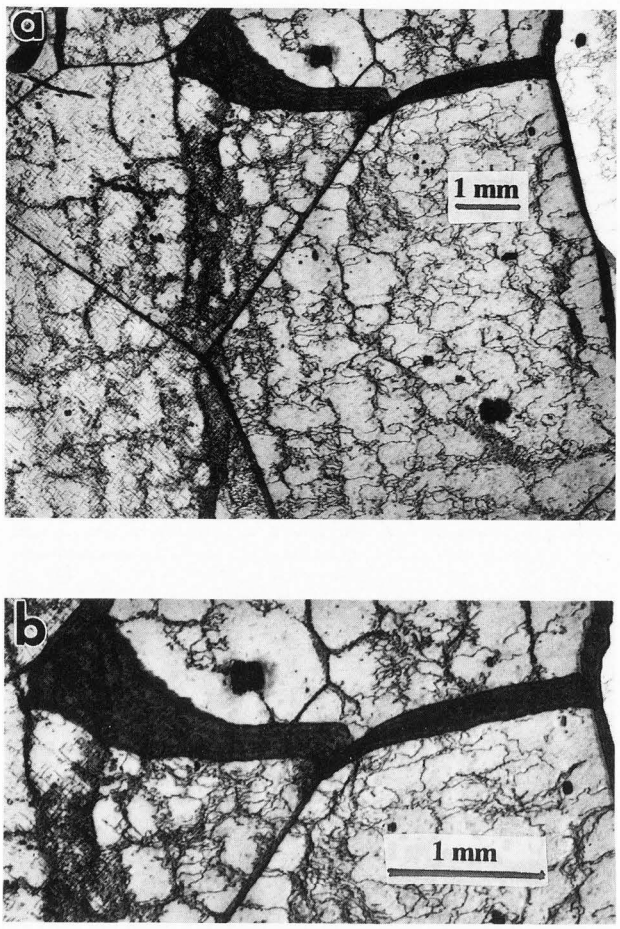

Figure 7. (**a**) Traverse topograph of a lithium fluoride crystal. 200 reflection. (**b**) Enlargement of the upper part of Figure 7a. Scale mark: 460 μm.

Bragg's law, is a very useful parameter in all discussions concerning the visibility of those defects which induce a rotation of the lattice planes and/or a change in the lattice parameter. Let $\Delta\Theta$ be the departure from Bragg's angle after the deformation. Then $\delta(\Delta\Theta) = \Delta\Theta' - \Delta\Theta$ is the local variation of the departure from exact Bragg's angle. Let d be the lattice spacing and α the angle by which the lattice planes are rotated around a certain direction (defined by the angle β it makes with the normal to the plane of incidence). Then:

$$\delta(\Delta\Theta) = \alpha\cos\beta - \frac{\alpha^2}{2}\tan\Theta + \frac{\Delta d}{d}\tan\Theta \qquad (9)$$

which can conveniently be expressed by introducing the atomic displacement $\vec{u}$ as:

$$\delta(\Delta\Theta) = -\frac{1}{k\sin 2\Theta_B}\,\vec{s}_h \cdot \vec{\nabla}(\vec{h}\cdot\vec{u}), \qquad (10)$$

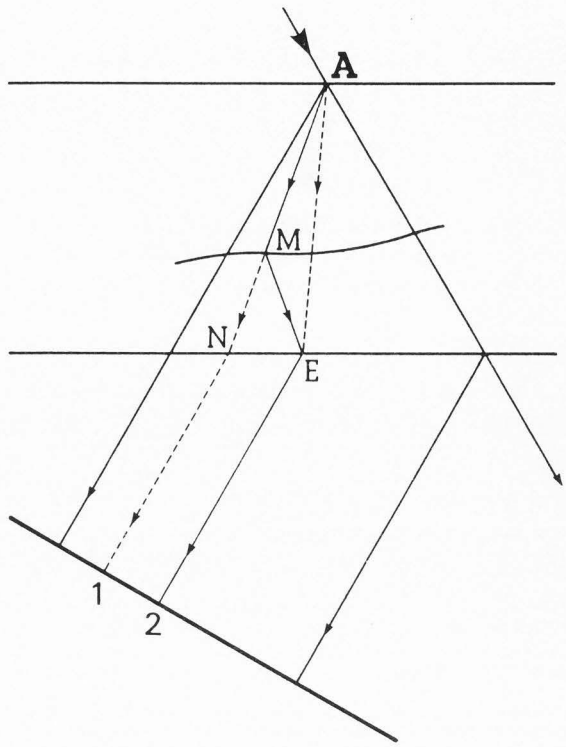

Figure 8. Formation of dislocation images in section topographs. 1: dynamic image; 2: intermediary image.

---

where $\vec{s}_h$ is the unit vector along the reflected direction.

Dislocations

In the vicinity of a dislocation, $\vec{u}$, the atomic displacement, is related to the Burger's vector $\vec{b}$:

$$\vec{u} = A\vec{b} + B\vec{b}_e + C\vec{b} + \vec{l}, \qquad (11)$$

$\vec{b}_e$ being the edge component of the Burger's vector and $\vec{l}$ a unit vector along the dislocation line itself. A, B, and C depend on the coordinates of the point where $\vec{u}$ is calculated.

Figure 5 qualitatively illustrates the criterion for the visibility of a dislocation in the case of a pure-edge and rectilinear dislocation. In the case illustrated by Figure 5a, $\vec{h}$ is parallel to $\vec{b}$, and the reflecting planes are greatly misoriented; $\vec{h}\cdot\vec{u}$ is maximum. In Figure 5b, $\vec{h}$ is perpendicular to $\vec{b}$, and the reflecting planes are less misoriented; the term involving $\vec{h}\cdot(\vec{b}\times\vec{l})$ still remains. Finally, in Figure 5c, $\vec{h}\cdot\vec{u} = 0$, and the reflecting planes are not misoriented. We therefore expect an intense image in the geometry corresponding to Figure 5a, a weak image in the geometry corresponding to Figure 5b and no image at all in the geometry corresponding to Figure 5c. By studying the way the contrast of a given image is changed, it is

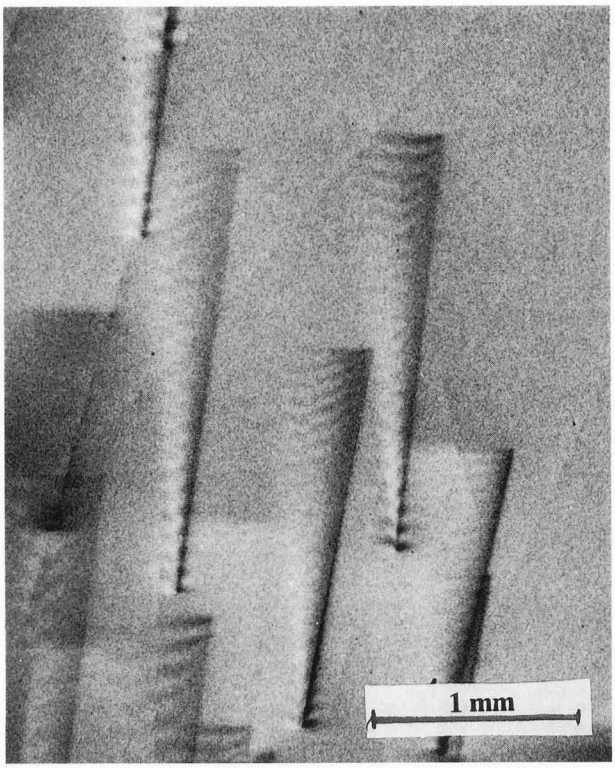

Figure 9. Traverse topograph: dislocation images. 200 reflection.

---

therefore possible to determine the direction of the Burger's vector of the dislocation. As for its length, it can usually be guessed from considerations on the crystal structure; computer simulations can then be useful in order to check a previous guess. Here, in Figure 5, we have considered different dislocations with different orientations and a fixed $\vec{h}$; in reality, the dislocation is given and the reflection vector $\vec{h}$ is changed. Although the Burger's vector of a pure edge or pure screw dislocation can be determined along this procedure, one may run into difficulties when dealing with a dislocation of a mixed-type.

Direct images [1, 11]

When the divergence Δ of the incident beam is large compared to that of the rocking curve (δ), only a small fraction of the beam is diffracted at the entrance surface, giving rise to wavefields which propagate inside the triangle ABC (Figure 6a). Most of the intensity of the incident beam (that which corresponds to a divergence which is larger than δ and smaller than Δ propagates along AB and is submitted to the ordinary photoelectric absorption process. If this part of the beam then intersects a dislocation line at D, the lattice planes which are severely disoriented around D will kinematically

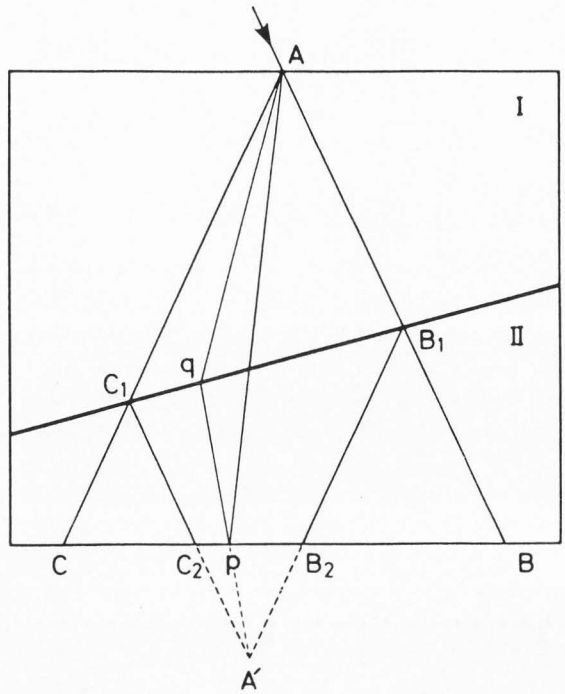

Figure 10. Wave-field propagation in a crystal containing a stacking fault. A': focal point of the new wavefields.

---

diffract the beam which will therefore propagate parallel to the reflected direction, i.e., parallel to AC. In this model, it is assumed that the impinging beam is kinematically diffracted inside a small volume such that

$$\delta\ (\Delta\Theta) > x\delta, \qquad (12)$$

where x stands for a parameter the value of which is close to 1.

The image then appearing (as a dark image) on the detection device (Figure 6b) is called the "direct image" of the dislocation. Figure 7 shows a topograph of a crystal of lithium fluoride separated in subgrains. Inside the grains, one observes individual dislocation images; these are direct images.

Dynamical images [2]

The propagation of wavefields inside a distorted crystal is submitted to the following rules:

- In the case of a weak deformation, the wavefield trajectories are no longer rectilinear but curved. Using Penning and Polder's theory, Malgrange [13] was able to state a qualitative but very useful rule which concerns the case of a constant value of $(\delta/\delta S_0)\ \delta(\Delta\Theta)$. This rule applies as long as the rotation of the lattice planes over a distance equal to Λ is not larger than $\delta/2$.
- In highly distorted regions, the concept of a wavefield which belongs to geometrical optics is no

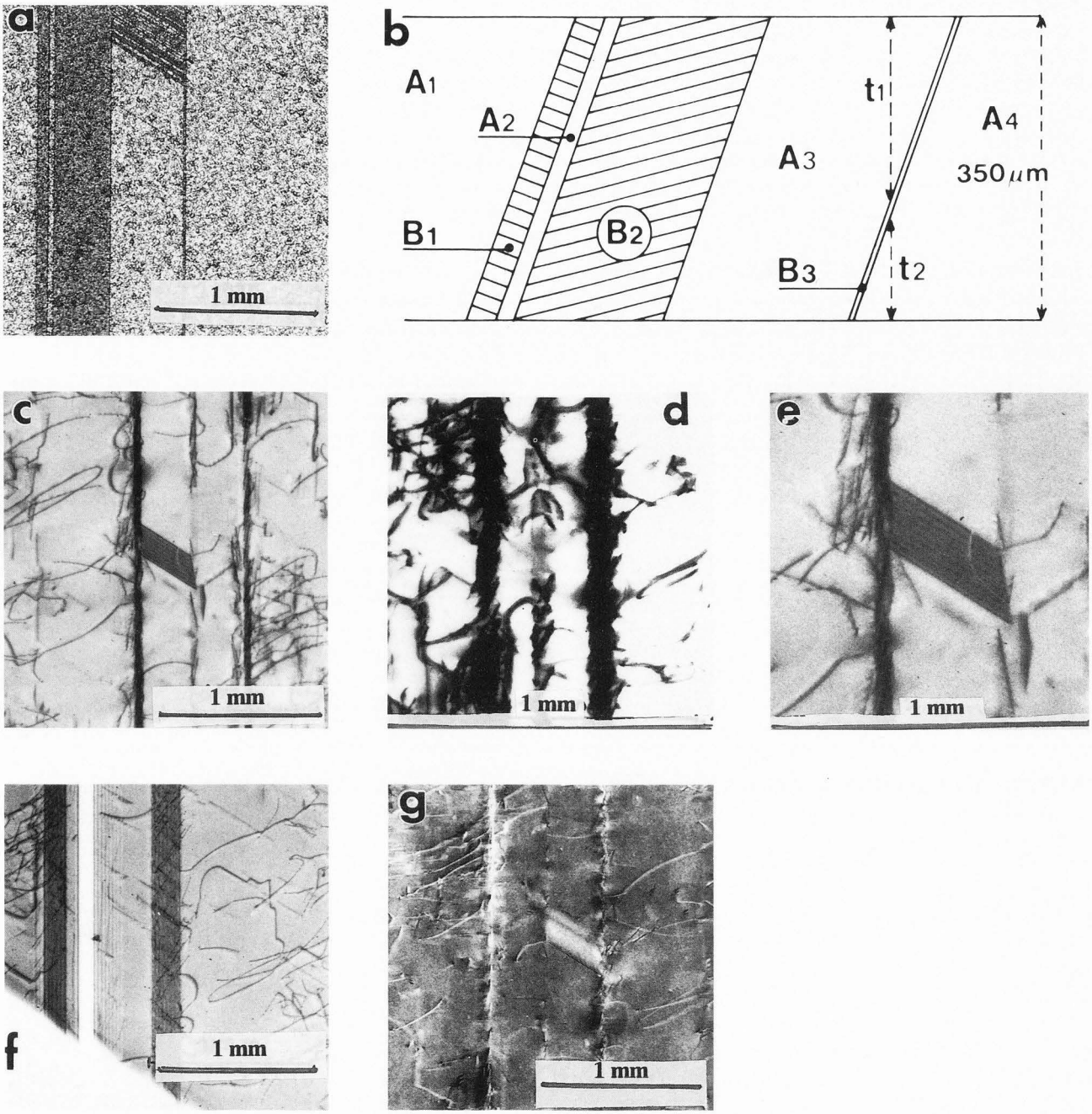

Figure 11. (**a**) Optical micrograph of the surface of a (111) silicon wafer. (**b**) Twin lamellae B_1, B_2, and B_3. (**c**) Traverse topograph: $\bar{1}11$ reflection; MoKα_1. (**d**) $\bar{3}\bar{3}3$ reflection; MoKα_1. (**e**) Enlargement of Figure 10c; scale mark: 150 μm. (**f**) $1\bar{1}1$ reflection. MoKα_1 (**g**) $\bar{1}11$ reflection; CuKα_1.

longer valid; diffraction phenomena then occur, resulting in the creation of new wavefields.

With these two rules, it is possible to explain, at least qualitatively, the formation of those images which are not direct images (see Figure 8). Since the ray which would have travelled along AN, if the crystal were perfect, now travels along a curved trajectory, one expects a lack of intensity in the corresponding direction AN. A white (or approximately white) image therefore appears at I on the photographic plate; its contrast is

important only if the value of $\mu_0 t$ is larger than 1 or even larger than 2. This contrast is usually called the "dynamical image". Besides, in the highly distorted region, right to the core of the dislocation, new wavefields are created; these propagate along directions, such as ME, which are different from the incident direction AM. At E, on the exit surface of the crystal, one expects interferences between those wavefields which have travelled along AME and those which have propagated directly along AE. Therefore, one observes, at 2, a new type of contrast, called the "intermediate image" which, under favorable conditions (adequate value of $\mu_0 t$, geometric features of the dislocation), appears as a set of fringes (Figure 9).

Phase shift contrast: Stacking fault

When the crystal is divided into two parts, I and II, by means of a stacking fault, part II is translated with respect to part I. The translation vector $\vec{f}$ characterizes this type of defect. From the diffraction point of view, this defect introduces a phase-shift $\alpha = 2\pi \vec{h} \cdot \vec{f}$ so that the h-coefficients in the Fourier expansion of the electric susceptibility are such that:

$$\chi_h^{II} = \chi_h^{I} e^{i\alpha}. \qquad (13)$$

The corresponding theoretical treatment has been achieved by Authier [2], assuming a spherical incident wave, a fixed crystal and a geometry of the Laue-Laue type (see Figure 10). A wavefield which propagates along Aq up to the interface then excites in part II a new wavefield which propagates along qp. The segment qp can be determined using the following procedures. From the two points B_1 and C_1 where the stacking fault intersects AB and AC, one draws a set of lines parallel to the transmitted and the reflected directions. The point where these lines intersect — call it A' — is the point where the new wavefields focus. The amplitude at p (on the exit surface of the crystal) of the reflected wave is a superposition of 8 terms: 2 normal wavefields (i.e., 4 terms) which have propagated along Ap and 2 new wavefields (i.e., 4 terms) which have propagated along qp.

The intensity at the exit surface is usually expressed as a sum of 3 terms:

$$I = I_1 + I_2 + I_3, \qquad (14)$$

where

$$I_1 = I_{perfect}[1 - |a| \sin^2\frac{\alpha}{2}], \qquad (15)$$

$$I_2 = b \sin^2\frac{\alpha}{2}, \qquad (16)$$

$$I_3 = c \sin^2\frac{\alpha}{2} + d \sin\alpha. \qquad (17)$$

This formula holds for points along B_2C_2 (Figure 10) since these points are reached by the new wavefields. Along BB_2 and C_2C, only I_1 should be taken into account. Note that I_1 is reduced as compared to what it would be, if the crystal were perfect; this reduction corresponds to the creation of new wavefields.

Each of these 3 terms gives rise to a set of fringes:

I_1: interference between normal wavefields;

I_2: interference between new wavefields; and

I_3: interference between normal and new wavesfields.

As can be seen on the above mathematical expression, only I_3 really depends on the sign of the phase-shift (via $\sin\alpha$). Besides, the only fringes which can be observed when the absorption is strong are those corresponding to I_3. On a traverse topograph and using a parallel slab, fringes of type I_1 disappear.

This discussion is summarized in Figure 11 where an example of these variations of the observed contrast is shown. A stacking fault lies in the region A_3 of the crystal. The plane of the stacking fault is parallel to $(1\bar{1}1)$. The image of this fault can be observed in Figure 11c (and even better in Figure 11e where it has been enlarged); the contrast is neither strong nor weak since μ_0 is $\cong 0.5$; the fringes corresponding to I_2 and I_3 are superposed. In Figure 11g, the fringes (I_3) are much contrasted but can be observed only on the exit surface since $\mu_0 t \cong 5$. In Figure 11d (3rd order reflection) and in Figure 11 f (the reflecting planes are parallel to the plane of the fault), the fault is out of contrast.

Since the first work by Kohra and Yoshimatsu [10] on stacking faults in silicon, many new results have been obtained, especially by Patel [16] who demonstrated how fruitful a mixed study which combines traverse and section topographs may be.

Quartz crystals

Specimen growth and sample preparation

The three quartz crystals under investigation have been chosen from the standard production of various companies. Specimen Q1, Q2, and Q3 were grown at the Toyo company (Japan), University of Peking (China) and SICN (France), respectively. From the initial bars, plates oriented parallel to (010) planes (commonly named Y-cut plates) were cut (Figure 12). After mechanical and chemical polishing, these samples, about 1 mm thick, were examined by X-ray transmission spherical wave topography and by planewave reflection topography.

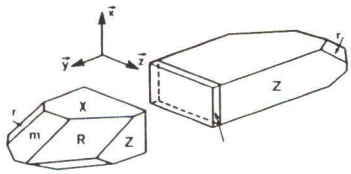

-a-

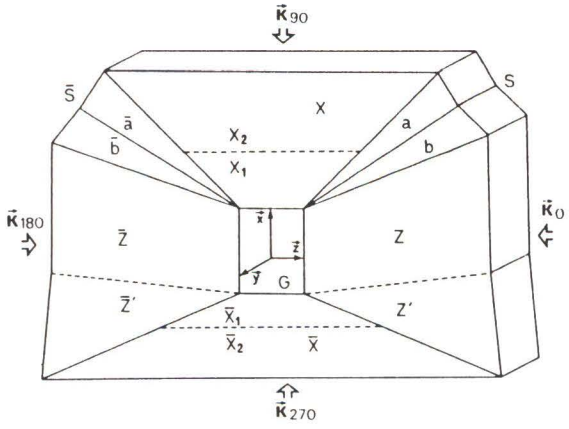

-b-

Figure 12. (**a**) Schematic drawing of a synthetic quartz crystal. The **X, Y, Z** orthogonal axis used in piezoelectricity. The Y-cut plates are cut perpendicular to the **Y**-axis. (**b**) Drawing of the various growth sectors or zones observed in the Y plates: X, Z, G (seed);. We have labelled K_0, K_{180}, K_{90}, and K_{270} the projections of the diffraction vectors following the four azimuths used for the plane-wave topography method.

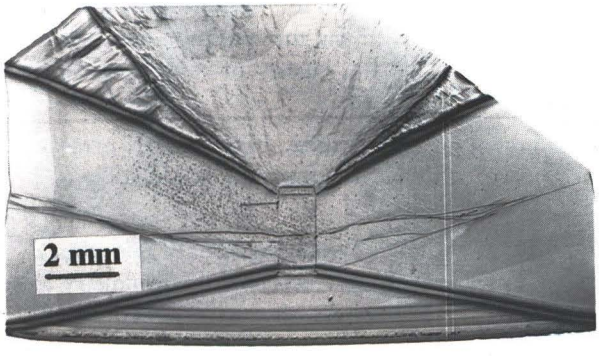

Figure 13. X-ray transmission topograph of the sample Q1; 100 reflection; MoKα_1. The seed G was cut in zone Z and presents very few dislocations in the different growth zones.

X-ray transmission topography

X-ray topographs of each of the three samples are presented in Figure 13 (Q1), Figure 14 (Q2) and Figure 15 (Q3). Some comparative remarks can be deduced from these topographs:

Crystal growth. These three samples show classical growth sectors [27]. However, a more detailed observation shows two Z' and $\bar{Z}$' sectors which are different from the usual Z zones.

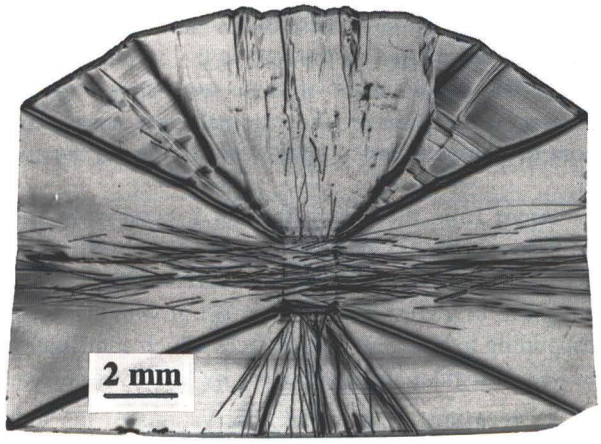

Figure 14. X-ray transmission topograph of the sample Q2; 100 reflection; MoKα_1. Note the important density of the dislocations in zone Z due to the dislocations present in the seed G. In zone X, we can note the bundles of the dislocations created on the seed. Two particular dislocations d and d' create rotations of the lattice in this sector X. In c, we can remark an unusual sector created at the end of the growth.

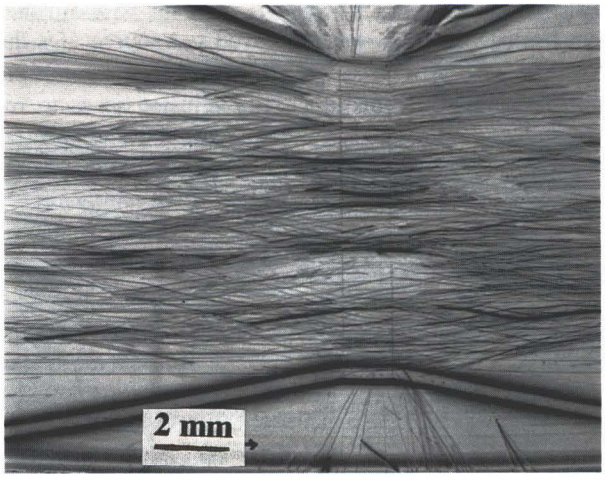

Figure 15. X-ray transmission topograph of the sample Q3; 100 reflection; MoKα_1. This central part shows that the seed G contains many dislocations which have been developed in the grown crystal.

As in the case of the two growth sectors a and b composing the S zones, these two Z' faces are of vicinal type and are initiated on the seed at the corners of the X face. The development of these two "faces" gives a reentrant angulation on the external final morphology more or less accentuated on the two Z sides of the crystal.

Apart from the classical a and b faces composing the S zones, the Q2 sample (Figure 14) presents a supplementary c vicinal face. Moreover, the X sector is composed of a great number of small growth zones corresponding to different vicinal faces which contribute to the very irregular form presented by this X "face".

Dislocations. From the observations of the topographs (Figures 13-15), it appears that all the seeds of the studied samples were cut in a Z zone of synthetic quartz. Following the sample, these three seeds contain few (Q1), several (Q2) or many (Q3) dislocations. This initial density of the dislocations is directly related to the final amount of these linear defects in the three samples.

Plane-wave reflection topography

Method. Plane-wave reflection topography was used for measuring local variations in lattice spacing and orientation in these Y-cut plates. For the experiments, synchrotron radiation was employed as a source. On the first axis of a double-axis spectrometer, a multiple reflection monochromator [17] is adjusted so as to release an extended wave of narrow angular and spectral divergence. The principal characteristics of this beam are [19]: $\lambda = 1.2378$ Å, $\Delta\lambda/\lambda = 7.10^{-6}$; intensity = 2.10^7 photons/cm^2/sec (1.72 GeV, 100 MA); and area = 1.5 x 1.5 cm^2. On the second axis, the sample, adjusted for the 040 reflection, is mounted. The Bragg angle is 35.6° and for this case, the calculated half-width of the rocking curve is 1.3 arc seconds for a perfect crystal. Four reflection profiles corresponding to four azimuth positions labelled 0, 180, 90, 270 have been recorded for all the three samples. Then, on different regularly spaced positions on each profile about ten topographs were obtained. An analysis of these series of topographs gives the $\Delta d/d$ values corresponding to the variations of the lattice parameter d (spacing of the (010) planes) and the $\Delta\Phi$ values corresponding to the rotations between each considered zone and a reference zone (Z sector in our case) by the following relations [26]:

$$\Delta\Phi_X = \frac{1}{2}(\Delta\Theta_0 - \Delta\Theta_{180}) \qquad (18)$$

$$\frac{\Delta d}{d} = -\frac{1}{2}\cot\Theta_B\,(\Delta\Theta_0 + \Delta\Theta_{180}) \qquad (19)$$

with:

- $\Delta\Theta_0$: angular difference between the position on the 0 profile where the considered zone gives the maximum intensity and the position where the reference zone has its intensity maximum;
- $\Delta\Theta_{180}$: Angular difference between the maximum intensity position for the same zone considered as for $\Delta\Theta_0$ but obtained from the 180 profile; and
- Θ_B: Bragg's angle.

We have also calculated the following values:

$$\Delta\Phi_Z = \frac{1}{2}\,(\Delta\Theta_{90} - \Delta\Theta_{270}) \qquad (20)$$

$$\frac{\Delta d}{d} = -\frac{1}{2}\cot\Theta_B\,(\Delta\Theta_{90} + \Delta\Theta_{270}), \qquad (21)$$

where $\Delta\Theta_{90}$ and $\Delta\Theta_{270}$ are obtained from the 90 and 270 rocking curves and topographs, respectively. In fact, the results concerning the $\Delta d/d$ should not depend on the considered azimuth coupled pairs but should allow for a comparison between the values obtained from the expression (8b) and (9b).

The $\Delta\Phi_X$ and $\Delta\Phi_Z$ notations and values are different because they refer to the calculated rotations around the X- and Z-axis. The 0-180 and 90-270 diffraction vector projections lie parallel to the Z- and X-axis, respectively, as is shown in Figure 12.

Reflection profiles. The profiles obtained for the three samples present different features for their half-width and for their maximum intensity. The experimental half-width is generally about 3 inches [7.6 cm; the theoretical value for the perfect crystal is 1.3 inches (4 cm)]. This is due to the fact that the crystal is not perfect and is composed of various growth sectors. Thus, the enlargement and the splitting presented by the profiles depend on the quality of the crystal and the different azimuths used.

Plane-wave topographs. Figures 16-18 present one profile and two typical topographs obtained for each of the studied samples.

Q1 sample. Two topographs of this sample are shown in Figure 16. We can note the symmetry about the X-axis of the contrast obtained for two equivalent sectors (Z and $\bar{Z}$ for example) and the quite perfect

---

Figure 16 (on facing page). (a) Reflection profile of the sample Q1 obtained for the azimuth 90. (b) Plane-wave reflection topograph corresponding to the position 24 on the reflection profile. The X and Z zone are out reflection in contrary to the S zones. (c) Plane-wave topograph corresponding to the position 21 on the profile. Note that only the X, Z and Z' zones and some part of the seed are in reflection.

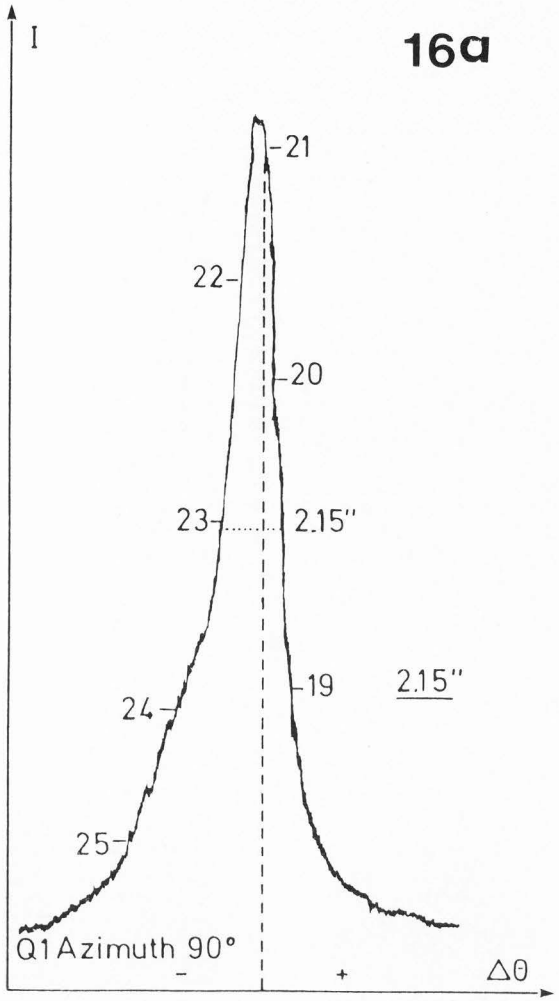

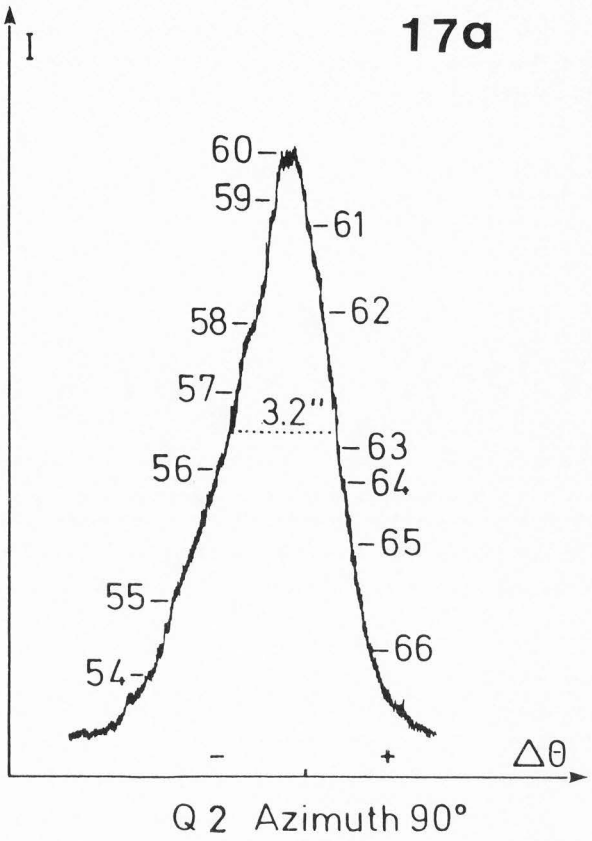

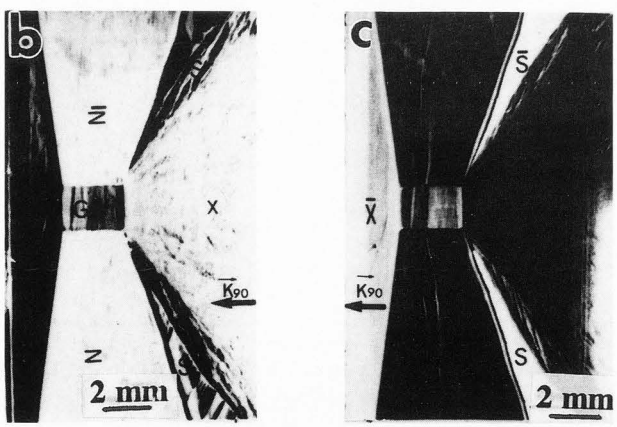

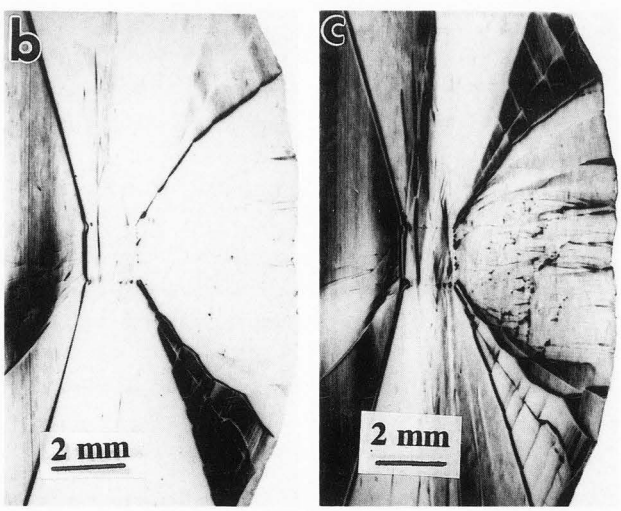

Figure 17. (**a**) Reflection profile of the sample Q2 obtained for the azimuth 90. Note that this profile is relatively large (3.2" or 8.1 cm). (**b**) Plane-wave topograph. Position 55 on the profile. The contrasts are complicated and do not present the symmetry about the X axis. Note the particular local contrast created by the dislocations d and d' in the X growth sector. (**c**) Planewave topograph. Position 57 on the profile. The contrasts are very complicated. We can note that the S zone is out of contrast, in contrary to the symmetrical S sector.

---

homogeneity of this contrast in the X, Z and $\bar{Z}$ zones.

These two features will not be verified for the two other samples (Q2 and Q3). The quantitative results

relative to this slice are given in the drawing of Figure 19 and are in good agreement with those obtained by Yoshimura *et al.* [26] for similar crystals also grown at the Toyo company.

Q2 sample (Figure 17). This plate shows two interesting features: (**1**) a very clear asymmetry of the contrast with respect to the X-axis essentially concerning the Z and $\bar{Z}$ zones; and (**2**) the lattice rotations due to the dislocations, particularly those situated between the Z and $\bar{Z}$ zones and the bundle of dislocations in the X sector. The values obtained for the deformations of the (010) planes in this plate are given in Figure 20.

Q3 sample. A profile and two topographs of this slice are given in Figure 18. The numerous dislocations give important deformations particularly in Z, $\bar{Z}$, Z' and $\bar{Z}$' zones and are at the origin of the heterogeneous contrast of these topographs. The complexity of the deformations is also revealed by the obtained four profiles which show very different half-width values [3.2", 2.5", 5.53" and 12" (8.1, 6.3, 14.0, and 30.5 cm) for the 0, 180, 90 and 270 azimuth positions, respectively], depending essentially on the lattice rotations created by the high density of the dislocations. The quantitative results relative to this slice are given in Figure 21.

Lattice parameter variations. The distribution of the lattice parameter of the (010) planes in the various zones with respect to the reference Z growth sector is quite similar over these three samples (Figure 19-21). Following the zones the $\Delta d/d$ is about 2×10^{-6} to 3×10^{-5}. However, some general features can be noted: (**1**) there is a good agreement between the obtained value for the seed G and the Z growth zone (reference). This result agrees with the quite good growth continuity of the samples from the seeds belonging to the Z zone; and (**2**) the S (a, b or c growth sectors), $\bar{S}$, and X growth zones show important lattice parameter variations with respect to the Z reference zone. These growth sectors correspond to "fast" faces and show important local parameter variations at the level of growth bands due to incorporated impurities.

Orientation variations of the lattice planes. One of the advantages of the technique of plane wave topography is related to the four azimuth settings used for this study. The rotations of the lattice planes can be analysed with respect to two perpendicular X- and Z-axes, and a precise analysis concerning the local deformations can be done. Concerning this point, the three samples show great differences due to localized individual defects (Figures 19-21).

Measurement precisions. Measurement couples 0-180 and 90-270 allow the control of the result validity obtained for the parameter variations $\Delta d/d$. Apart from

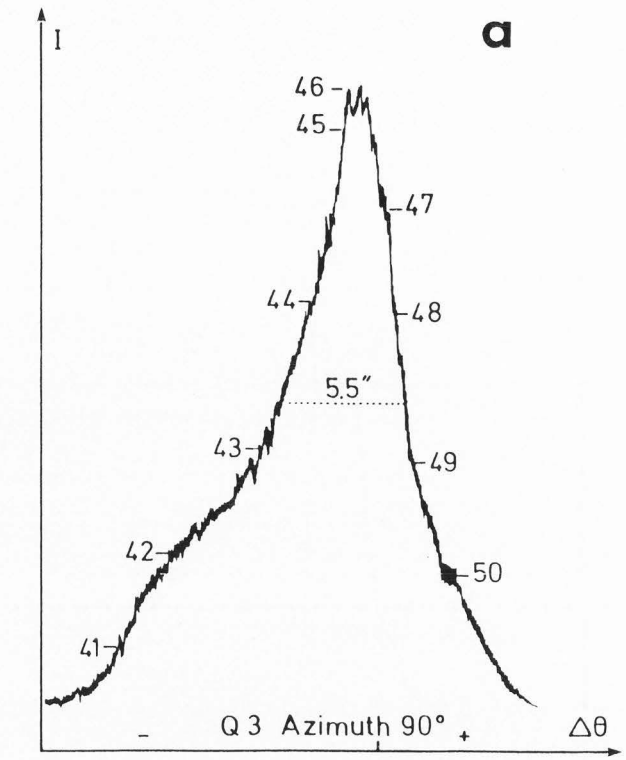

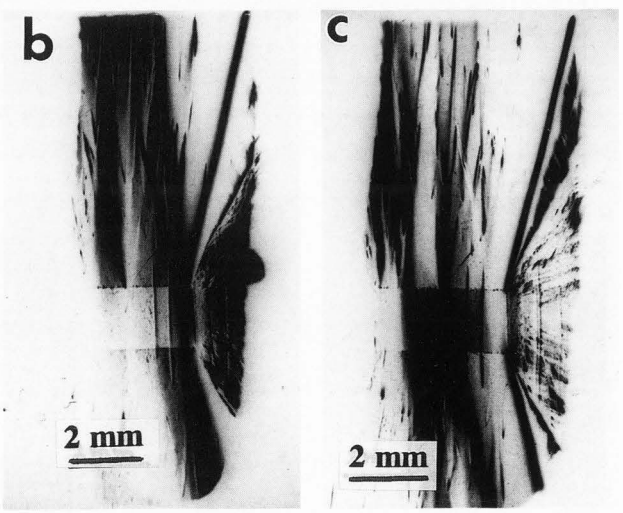

Figure 18. (**a**) Reflection profile of the sample Q3 obtained for the azimuth 90. This broad profile is due to the great inhomogeneity of the crystal. (**b**) Plane-wave topograph. Position 44 on the profile. We can note the great density of the dislocations which create great deformations in the Z sectors. The X sector presents a good contrast while the S zones are out of contrast. (**c**) Planewave topograph. Position 47 on the profile. The deformations due to the dislocations in the Z zones are very complicated.

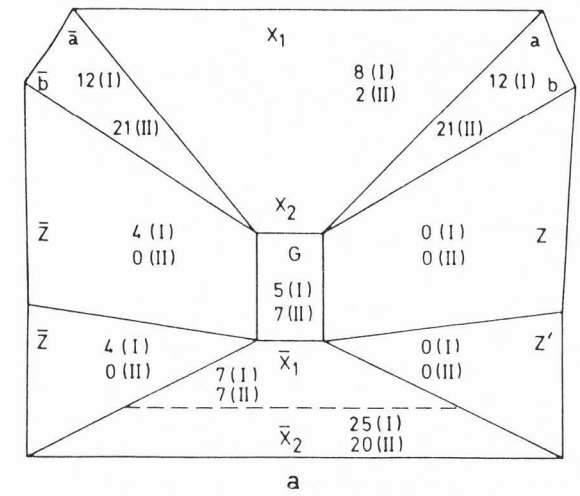

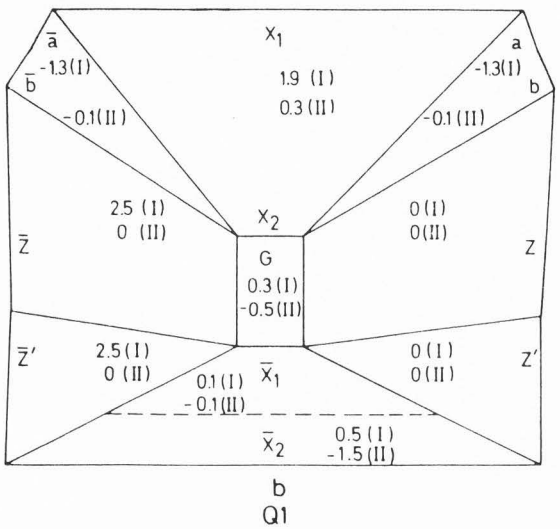

Figure 19. Sample Q1. (**a**) Results of the calculations obtained in the various zones concerning the variations of the parameter ($\Delta d/d$) (x 10^6) from the plane-wave reflection topographs. The comparisons of the results obtained from the relations (1b) and (2b), respectively, noted (I) and (II) are in good agreement. (**b**) Results of the disorientations $\Delta\Phi$ (in arc seconds) obtained from the (1a) and (2a) relations, respectively, and corresponding to the rotations about the X-axis (I) and Z-axis (II).

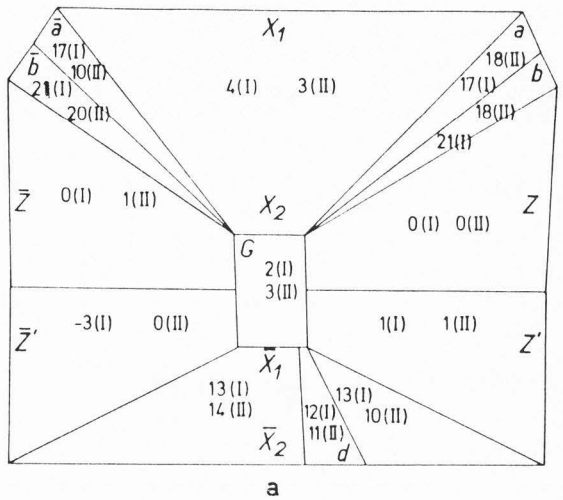

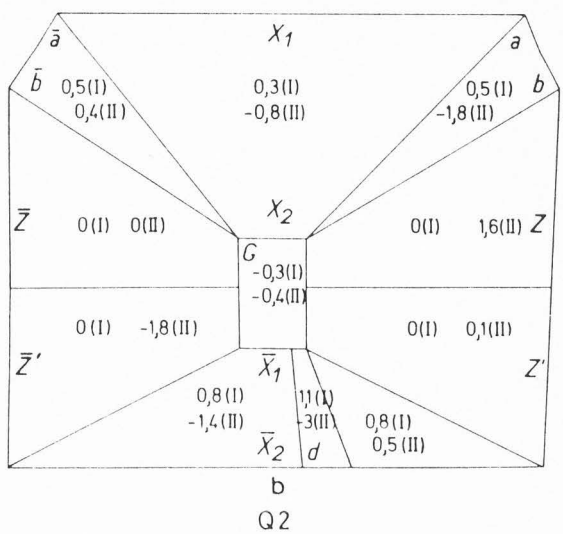

Figure 20. Sample Q2. (**a**) Results of the calculations obtained for the ($\Delta d/d$) (x 10^6). (**b**) Results of the rotations $\Delta\Phi$ (in arc seconds) about the X-axis (I) and Z-axis (II). We can note important rotations of the lattice with respect to the Z reference sector. The d and d' dislocations (in the X zone) induce rotations about the X-axis. The part bounded by these two dislocations presents a value of rotation different from these obtained at the outside of this zone.

---

some results, the agreement is generally satisfactory. The important sources of errors are due to several factors: (**1**) the precision on the maxima of intensity is variable following the sample and is related to the homogeneity more or less effective in the various growth zones; and (**2**) the stability of the setting during the exposure of the film and correlatively the quality of the mounting which can change from an experiment to another one.

These factors contribute to an imprecision for the obtained results which we have estimated to 5 x 10^{-6} for $\Delta d/d$ and about 0.2" (5 mm) for $\Delta\Phi$ in the X, Z, $\bar{Z}$ and Z' sectors. For the sectors where the lattice parameter variations are important (X, S, $\bar{S}$) and which correspond to positions located on the sides of the profiles, the

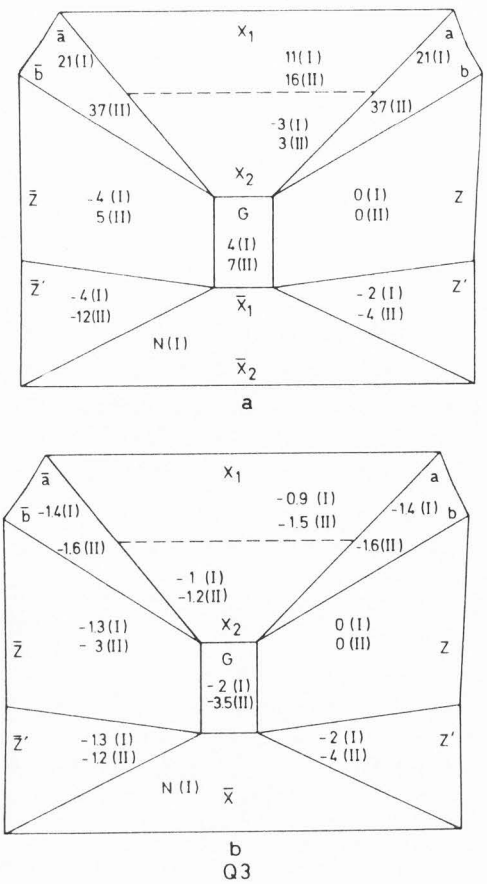

Figure 21. Sample Q3. (**a**) Results of the calculations obtained for the ($\Delta d/d$) (x 10^6). (**b**) Calculations of the rotations $\Delta\Phi$ (in arc seconds) of the various zones about the X-axis (I) or the Z-axis (II). The reference zone is the Z sector.

---

lattice parameter variations were estimated at 8 x 10^{-6} and the rotations at 0.5" (1.25 cm).

Stroboscopic topography

Experimental techniques [4]

Synchrotron radiation from storage ring has a time structure because the circulating particles are concentrated in bunches. Two fixed parameters of this time structure are the circulation time of an individual bunch and its length. For DCI (double collision in the igloo; Orsay, France), these values are 315 ns and 1 ns. Another variable parameter, in some other cases, is the number of stored bunches but in our experiments this number is always 1 because the storage ring of DCI was running in single-bunch mode.

The setting of the experiment is composed of two

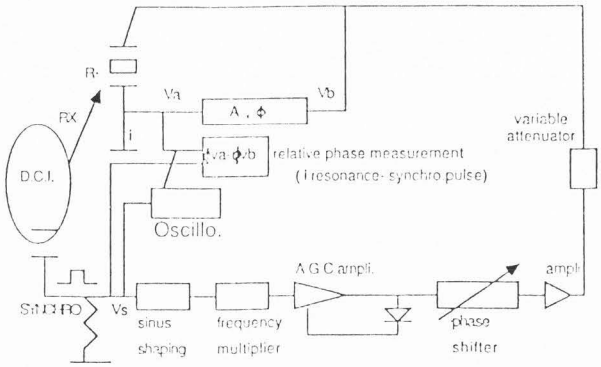

Figure 22. Set-up of the stroboscopic topography.

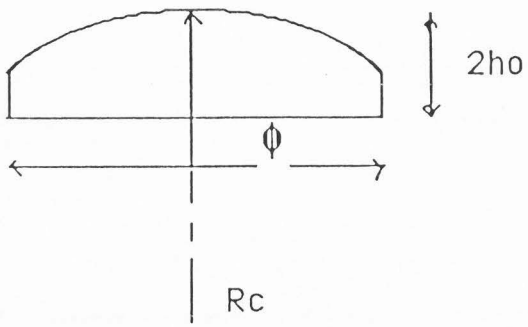

Figure 23. Drawing of a plano-convex resonator.

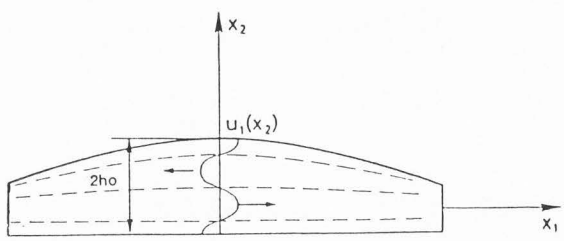

Figure 24. Representation of the deformations due to the thickness shear mode in an AT-cut plano-convex resonator.

---

parts:

Topographic setting. The topographic setting is quite simple because the topographic station at LURE (Laboratoire pour l'Utilisation du Rayonnement Synchroton, Orsay, France) is equipped with a double-axis spectrometer. This spectrometer permits, when the quartz sample is placed in the incident (white) beam, one to obtain a Laue pattern of topographs [24]. This setting is simple because the resonator, mounted on a goniometer head with a support adapted for the frequency adjustment is placed perpendicular to the beam without

Table 1. Results of stroboscopic experiments.

	Resonance frequency (MHz)	Mode (overtone)	Rc (mm)	F (mm)	2ho (mm)
Q1	3.169280	Third	150	15	1.592
Q2	6.338560	Fifth	150	15	1.322
Q3	6.338560	Fifth	150	15	1.322

precise adjustment. However, the most interesting aspect of this spectrometer is the monochromatic setting. In this case, the first axis holds a (110) sample of germanium which is adjusted to select only one wavelength from the white beam. The 220 reflection was chosen and the wavelength of the beam on the second axis was 0.7 Å for a Bragg angle $\Theta = 10.08°$. From the resonator, adjusted on this axis, monochromatized images were obtained. By the use of a very fine slit, we also obtained "section" topographs.

Electronic control. To obtain an exact synchronization of the X-ray pulses and of the piezoelectric vibration of the resonators, a pulse signal obtained from the positron bunch (by a capacitive pick-up) is used to generate the excitation signal of the resonators. This signal is shaped in a sinusoidal form by filtering at the recurrence frequency ($f_0 = 3.169280$ MHz) or at an harmonic of this frequency (nf_0 with $n = 2, 3,...$). A phase shifter permits one to vary the relative phase between the synchropulse and the sinusoidal signal used to excite the resonance of the crystal (after a level adjustment).

To have an exact resonance condition (resonator voltage in phase with resonator current) the resonators were adjusted by metallization to have frequencies very close to f_0 (or nf_0). A fine adjustment (a few Hertz) is made with a large serial variable capacitance.

The electrical parameters of the resonator are measured, in-situ, with a vector voltmeter (level of excitation, verification of the zero phase resonance condition). Another vector voltmeter is used to monitor the relative phase angle between the resonator current (or voltage) and the synchronization pulse. After calibration, this relative phase between the resonator current and the X-ray pulse (RPCX) is known with a precision of about 3° with most of the uncertainty resulting from the effects of the temperature fluctuations on the resonator.

The general principle of the set-up is given in Figure 22.

Experiments

The purpose of this study was to determine the role of defects on the acoustical vibrations.

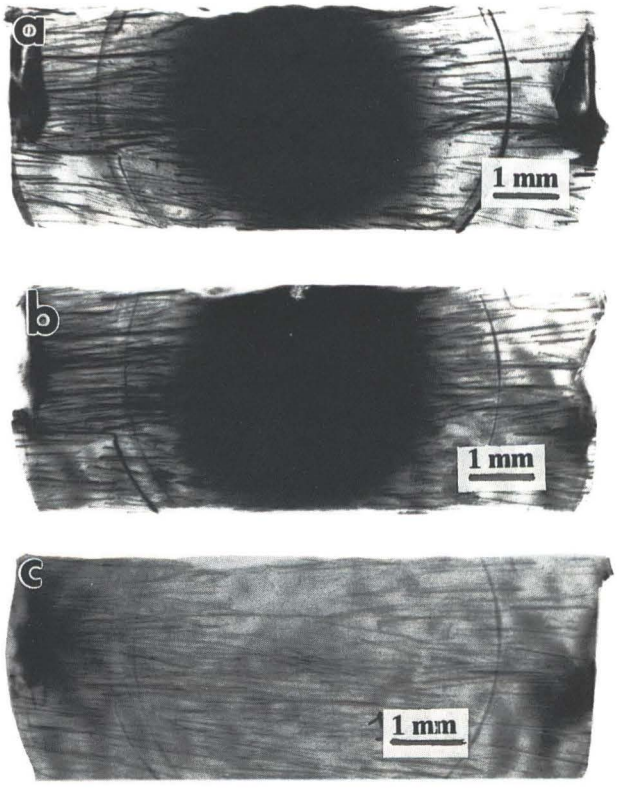

Figure 25. Three X-ray topographs obtained from the same Laue pattern. (**a**) The central black contrast which depends on the u_1 component of the deformation is clearly visible for the $11\bar{2}$ reflection. (**b**) The black contrast is also visible for the $2\bar{2}3$ reflection. (**c**) $0\bar{1}3$ reflection. The contrast vanishes. For this reflection $\bar{h} \cdot \bar{u} = 0$.

In the stroboscopic experiments the samples were plano-convex resonators having the basic design of high Q factor 5 MHz, 5th overtone resonators (Table 1). The first resonator Q1 made with a premium Q quartz was operated at the third overtone at the synchrotron frequency. The second Q2 and the third with Q3 crystals were made with premium Q synthetic Quartz and with natural crystal, respectively. They were operated as fifth overtone at two times the synchrotron frequency (Figure 23).

All resonators were electroplated with Cr/Au metallization (electrode diameter 8 mm; mass loading = 1%).

As established by the theory [23], the used vibration modes are much more trapped in the case of Q2 and Q3 than for Q1.

The dominating vibration mode in the AT-cut is the thickness-shear mode which corresponds to a standing transverse wave in the crystal (Figure 24). The planes parallel to the surface are displaced in the X_1 direction

leading to a sinusoidal shear of planes perpendicular to the X_1-axis.

The components u_2 and u_3 of the displacement are generally weak in regard to the u_1 component when no coupling to flexure or planes occurs.

On the X-ray topographs, the most important contrast located under the electrodes is due to the u_1 component and depends on the level of the amplitude of the vibration applied on the crystal. This contrast depends also on the diffraction conditions. Particularly, when the product $\vec{h} \cdot \vec{u}$, where $\vec{h}$ is the reflection vector and $\vec{u}$ the displacement due to the deformation, give zero, the contrast due to the deformation vanishes.

In our cases, the most important u_1 component of the displacement was along the (100) direction. Then, on the topographs corresponding to the (0kl) reflecting planes the contrast of the deformation did not appear.

Observation

Different types of X-ray topographs have been obtained varying the RPCX, the level of the input signal and the topographic setting (Laue, monochromatic, section topographs, etc.). We shall only report the most important observations we have obtained for the studied resonators [28].

Q1 resonator. In Figure 25, we present three topographs of the same Laue pattern obtained for 120° RPCX and a power of 0.9 mW. It can be observed that, depending on the reflection, the contrast due to the deformation changes. The central black contrast which depends on the u_1 component of the deformation is clearly visible for the $11\bar{2}$ (Figure 25a) and $2\bar{2}3$ (Figure 25b) reflections but vanishes for the $0\bar{1}3$ reflection (Figure 25c). For this reflection, $\vec{h} \cdot \vec{u} = 0$ and the contrast (broad fringes) due to the u_3 component of the deformation is more visible.

Figure 26 presents two topographs of the crystal obtained for $11\bar{2}$ reflection for two different RPCX (with the same vibrating level). For 90° RPCX (Figure 26a), the crystal presents a very similar contrast to that obtained without vibration because the diffracting planes are not deformed. The high density of the dislocations oriented parallel to the **C** crystallographic axis can be observed. The faint circular contrast is due to stresses in the electrode metallization. The effects of the dislocations on the vibration mode are shown in Figure 26b (and also in Figures 25a and 25b) where it can be obviously seen that the zone of vibration does not have the quasi-circular symmetry expected and that where a large density of the dislocations exists they unconfine the mode. This was also observed elsewhere by conventional X-ray topography (continuous exposure during the vibration).

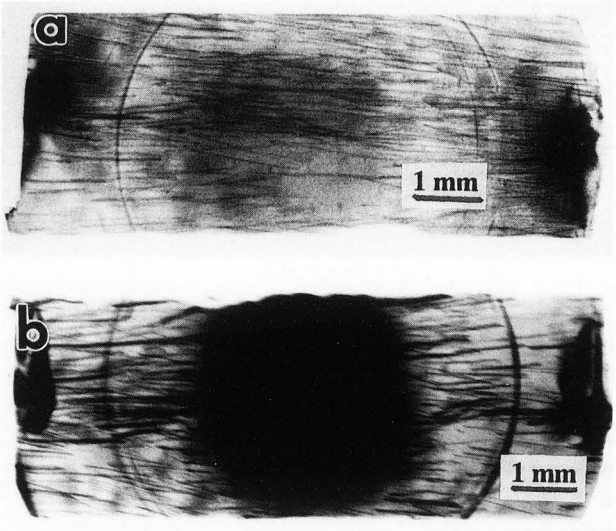

Figure 26. Two topographs of the same crystals obtained for two different RPCX. (**a**) 90° RPCX. No vibrations are observed. (**b**) The dislocations unconfine the mode of vibration.

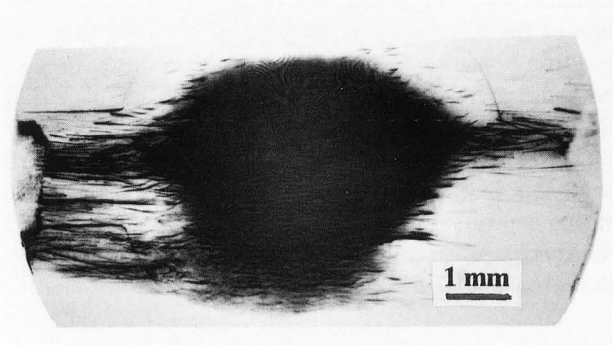

Figure 27. Monochromatic topograph; $2\bar{1}0$ reflection. The dislocations unconfine the mode. It can be observed in the central zone fringes of "moiré" type.

The same feature can be observed on the monochromatic topographs. In Figure 27, a monochromatic topograph ($2\bar{1}0$ reflection) of the same resonator shows another interesting contrast in the central resonating zone: fringes of "moiré" type appear, and their configurations change with the RPCX. These fringes are due to interferences between X-ray wavefields propagating in the crystal. They are generally located at the level of the dislocations and probably characterize very locally deformed zones.

Q2 resonator. This crystal is characterized by a better confinement of the vibration. The four monochromatic topographs presented in Figure 28 were obtained varying the level of the input signal (without vibration in Figure 28a, 15 mW in Figure 28b, 35 mW in Figure

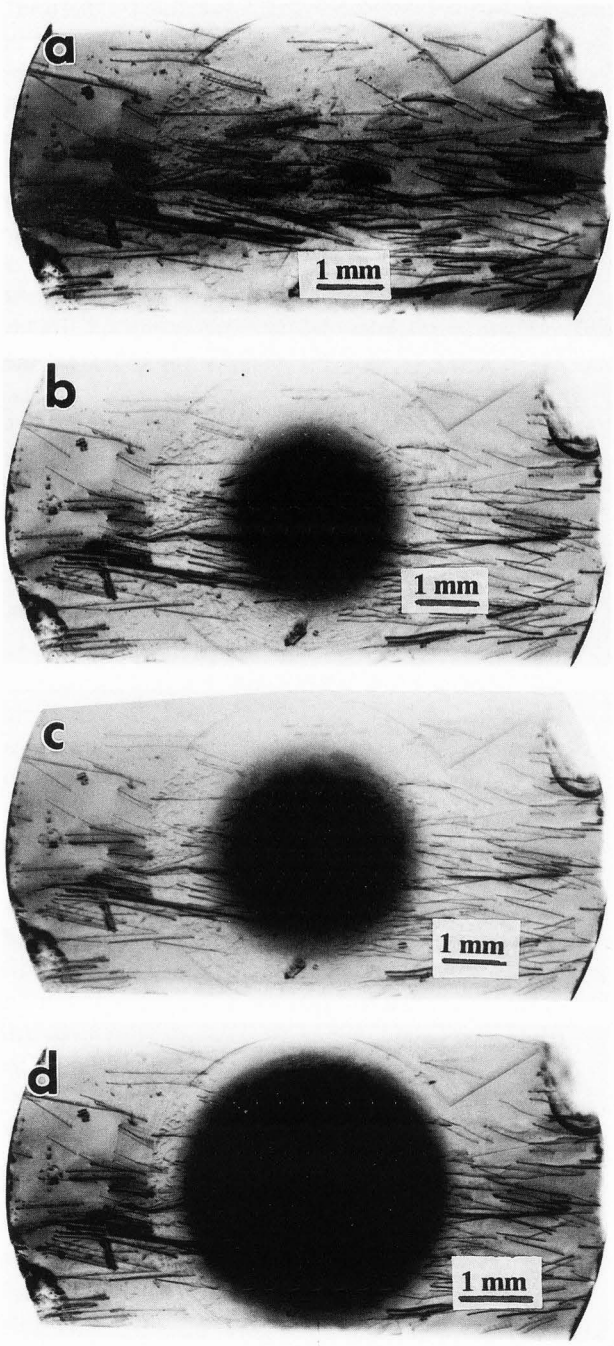

Figure 28. Four monochromatic topographs obtained varying the level of the input signal. (**a**) Without vibration. (**b**) 15 mW. (**c**) 35 mW. (**d**) 350 mW.

28c, and 350 mW in Figure 28d). The density of the dislocation in this crystal is less important than in the previous one. However, the "moiré" type fringes are visible in the central part at the level of the dislocations. Their configuration varies with the RPCX.

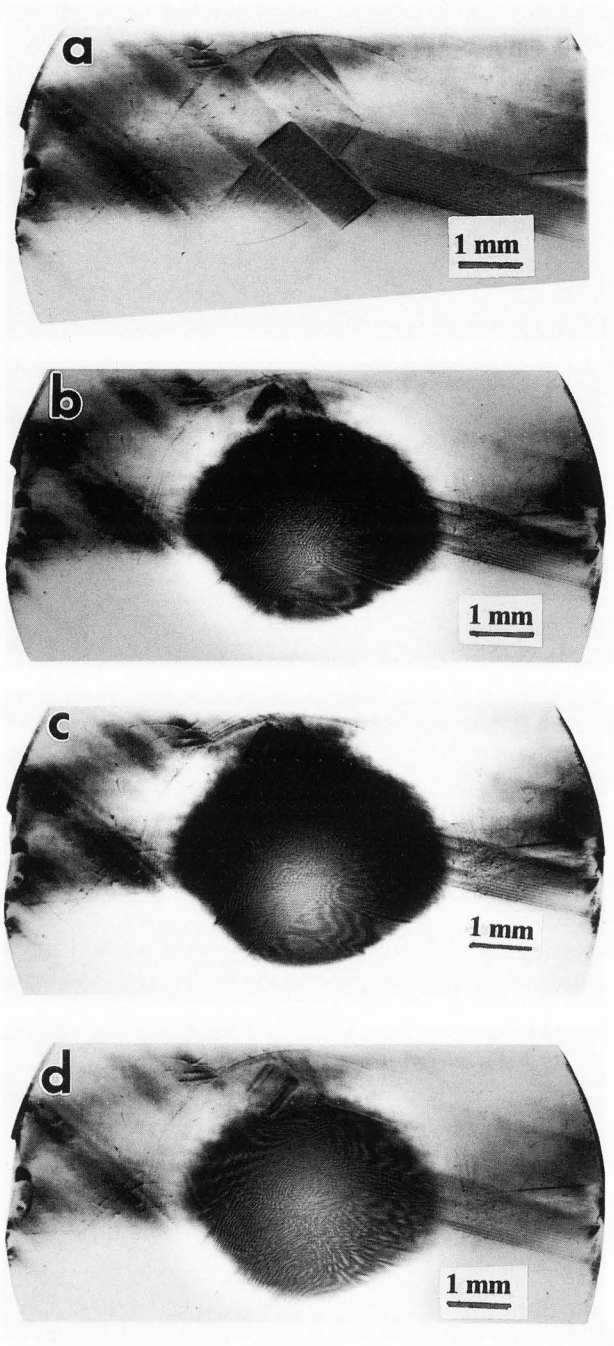

Figure 29. Four monochromatic topographs of the same resonator. (**a**) Without vibration. (**b**) 45° RPCX. (**c**) 0° RPCX. (**d**) 135° RPCX. It can be observed that the growth bands changes the confinement the mode of vibration.

The geometrical aspect of the central vibrating zone seems less deformed than the vibrating part of the Q1 crystal. For the Q2 resonator it appears, due to their lower density, that the influence of the dislocations is less important. On the other hand, circular fringes lo-

cated between the black contrast and the edge of the electrodes present a contrast which varies with the RPCX. They are also due to interferences of the propagating wavefields in the crystal but reveal a probable secondary mode of vibration.

Q3 resonator. Four monochromatic topographs are presented in Figure 29. The last three were obtained with the same level of the vibration (90 mW) but for different RPCX (45° in Figure 29b, 0° in Figure 29c and 135° in Figure 29d). The topograph in Figure 29a was obtained without vibration. This crystal is a natural one, and the defects present are only growth bands.

This crystal shows different interesting features:

- The central black zone presents a contrasted part which depends on the RPCX;
- This is also verified for the "moiré" type fringes which configuration changes between Figures 29b-29d;
- The external circular fringes (between the vibrating zone and the edge of the electrodes) appear only when the crystal is vibrating and seem to be invariable when the RPCX changes; and
- The growth bands seem to have a very less important effect on the lateral confinement of the vibration mode than the dislocations do.

To summarize the different observations, it can be said that the global effect of the dislocations in AT-cut resonators is to decrease the lateral confinement of the thickness shear mode when their density is important (more than 10^2 to 10^3 per cm^2). The dislocations seem to increase the phase velocity of the shear mode locally and therefore to contribute to the local untrapping of a confined mode. This hypothesis appears to be reinforced by the observed fact that bunches of dislocations of similar orientations constitute a guiding structure for the shear wave at the periphery of the vibration mode. This permits one, in the case of weakly trapped modes, to observe an important untrapping effect. Although no direct experimental evidence of this phenomenon has yet been obtained, one can wonder whether the dislocations, like other elastic discontinuities, may or not may introduce some mode conversion (fast shear to slow shear or longitudinal).

Additionally, the higher impurity level in the growth band may also introduce local variations of the phase velocity of the shear mode, leading to an increase (or to a decrease) in the energy trapping parameters locally. However, due to the complexity of the growth bands structure of the studied sample, no simple conclusion about this point can be drawn at this time.

The technique of the Laue Stroboscopic topography can directly reveal the different modes of the vibration by visualization of all the components of the (instantaneous) deformation [28]. "Moiré" type fringes show local deformations (associated with the defects which seem to induce perturbations in the vibration modes). "Section" topographs indicate the depth of the acoustic contrast in the studied crystal (the area with the maximum curvature of planes). It is most probable that the deformations of the "moiré" fringes (produced by an X-ray interference process not already fully elucidated) correspond to local modifications of the transverse wave shape resulting from the influence of the defects (surface defects appear to produce similar defects). The stroboscopic method can also permit one to obtain other information about piezoelectric resonators such as information relative to the localization of acoustic dissipations, or to the influence of imperfect geometries of the surfaces. Further experiments are requested, with resonators exhibiting different dislocation densities and different energy trapping parameters, to gain a full understanding of the importance of the interactions of defects with vibration modes.

Conclusion

The purpose of this paper was to discuss some elements of dynamical theory and to introduce some basic ideas on defect image formation. Since only a few types of defects have been considered, the reader should go further into the subject with, for example, Tanner's monograph on X-ray Diffraction Topography [21].

The analysis of the X-ray spherical wave topographs of various Y-cut plates of synthetic quartz crystals has shown that the coherence of the lattice between the seed and the grown crystal, following the (010) planes, is directly related to the density of the dislocations present in the seed. For three samples, the local deformations are essentially related to the density of the dislocations. The plane-wave topography has shown that the local deformations can be estimated with good precision and related to the growth defects.

The time structure of synchrotron radiation enables Stroboscopic X-ray topography, and with the use of the beam delivered at LURE, we have examined three quartz resonators. By the use of different topographic settings, several types of vibration modes and the perturbations due to the defects have been observed. Defects such as growth bands and especially dislocations disturb the BAW (bulk acoustic wave) propagation in the crystals and can induce losses by untrapping a part of the energy of the mode conversion. However, the topographic contrast due to the propagation of X-ray wavefields in the deformation fields of acoustic waves, is not well understood, and calculations of the beam trajectories in the crystal and simulation of topographs will be necessary to explain the observed contrasts.

Acknowledgments

The author thanks the group of Profs. A. Authier and J.F. Petroff for providing several topographs and M. A. Jeanne-Michaud for their reproduction.

References

[1] Authier A (1967) Contrast of dislocations images in X-ray transmission topography. In: Advanc. X-ray Anal. Newkirk JB, Mallet GR (eds.). Plenum Press, New York. **10**, 9-31.

[2] Authier A (1978) Contrast of images in X-ray topography. In: Diffraction and Imaging Techniques in Material Science. Vol. II. Amelinkx S, Gevers R, Remaut G, van lan Duyt J (eds.). North-Holland, Amsterdam. 481-520.

[3] Bond WL, Andrus J (1952) Structural imperfections in quartz crystals. J. Am. Mineralogist **37**, 622-632.

[4] Cerva H, Graeff W (1984) Contrast investigation of surface acoustic waves by stroboscopic topography. I. Orientation contrast. Phys. Stat. Sol. **A82**, 35-45.

[5] Ewald PP (1917) Zur begrundung der kristalloptik. III. Die kristalloptik der Rontgenstrahlen (Fundamental basis of crystal optics. III. Crystal optics of X-rays). Ann. Physik. **54**, 519-597.

[6] Kato N (1964) Pendellosung fringes in distorted crystals. II. Application to two beam cases. J. Phys. Soc. Jap. **19**, 67-77.

[7] Kato N (1964) Pendellosung fringes in distorted crystals. III. Application to homogeneously bent crystal. J. Phys. Soc. Jap. **19**, 971-985.

[8] Kato N (1968) Spherical waves theory of dynamical X-ray diffraction for absorbing perfect crystal. I. The crystal wave fields. J. Appl. Phys. **39**, 2225-2230.

[9] Kato N (1968) Spherical waves theory of dynamical X-ray diffraction for absorbing perfect crystal. II. Integrated reflection power. J. Appl. Phys. **39**, 2231-2237.

[10] Kohra K, Yoshimatsu M (1960) X-ray observations on cleavage faces of LiF single crystals. J. Phys. Soc. Jap. **15**, 1760-1770.

[11] Lang AR (1959) The projection topograph: A new method in X-ray diffraction microradiography. Acta Crystal. **12**, 249-250.

[12] Lang AR (1980) Defect visualisation: individual defects. In: Characterization of Crystal Growth Defects by X-ray methods. Tanner BK, Bowen DK (eds.). Plenum Press, New York. 161-185.

[13] Malgrange C (1969) Etude expérimentale de la propagation des rayons-X dans des cristaux parfaits déformés sous l'action d'un gradient thermique. (Experimental study of X-ray propagation in deformed perfect crystals under a thermic gradient). Acta Cryst. **A25**, 356-363.

[14] Matsushita T (1974) A method of obtaining a highly parallel and monochromatic X-ray beam by successive diffraction. J. Appl. Cryst. **7**, 254-259.

[15] Miltat J, Sauvage-Simkin M (1984) Synchrotron radiation imaging techniques. A review. In: Applications of X-ray Topographic Methods To Materials Science. Weissman S, Balibar F, Petroff JF (eds.). Plenum Press, New York. 185-209.

[16] Patel JR (1981) Defects in silicon. In: Semiconductor Silicon 1981. Ruff HR, Sirtl E (eds.). Electrochemical Society, Princeton, NJ. 71-92.

[17] Petroff JF, Sauvage M, Riglet R, Hashisume M (1980) Synchrotron radiation plane-wave topography. I. Application to misfit dislocation imaging in III-V heterojunction. Phil. Mag. **A42**, 319-327.

[18] Penning P, Polder D (1961) X-ray topography. Philips Res. Reports **16**, 419-427.

[19] Sauvage M, Petroff JF (1980) Use of synchrotron radiation for X-ray topography. In: Synchrotron Radiation Research. Winick H, Doniach S (eds.). Plenum Press, New York. **18**, 607-638.

[20] Takagi S (1962) Dynamical theory of diffraction applicable to crystals with any kind of small distortion. Acta Cryst. **15**, 1311-1312.

[21] Tanner BK (1976) X-ray Diffraction Topography. Pergamon Press, Oxford. 1-174.

[22] Taupin D (1964) Théorie dynamique de la diffraction des rayons-X par les cristaux déformés. (Dynamical theory of X-ray diffraction in deformed crystals). Bull. Soc. Fr. Mineral. Cryst. **87**, 469-511.

[23] Tiersten HF, Smythe RC (1979) Analysis of contoured resonators operating in overtones of coupled thickness shear and thickness twist. J. Acoust. Soc. Amer. **65**, 1455-1460.

[24] Tuomi T, Naukkarinen K, Rabe P (1974) Use of synchrotron radiation in X-ray topography. Phys. Stat. Sol. **A25**, 93-106.

[25] Von Laue M (1960) Röntgenstralinterferenzen (X-ray Interferences). Akad. Verlags Gesellschaft. Frankfurt, Germany. 25-38.

[26] Yoshimura J, Miyazaki T, Wada T, Kohra K, Hosaka M, Ogawa T, Taki S (1979) Measurement of local variations in spacing and orientation of lattice planes of synthetic quartz. J. Cryst. Growth. **46**, 691-700.

[27] Zarka A, Liu Lin, Buisson X (1981) Influence de la localisation se chorielle du germe su la qualité cristalline du quartz de synthetic. (Effect of the localization of the seed on the crystal quality of synthetic quartz). J. Cryst. Growth **54**, 394-398.

[28] Zarka A, Capelle B, Detaint J, Schwartzel J (1988) Stroboscopic X-ray topography of quartz resonators. J. Appl. Cryst. **21**, 967-971.

Discussion with Reviewer

F. Hasselbach: Which types of lattice defects can be detected by X-ray transmission topography? What is the resolution of this method compared to transmission electron microscopy?
Author: Only extended defects like dislocations, growth bands, stacking faults or precipitates can be detected by X-ray transmission topography. The resolution obtained by X-ray transmission topography is very poor in comparison with that obtained by electron microscopy. It is about 3 to 5 μm.

F. Hasselbach: By "plane-wave reflection topography" is it possible to detect lattice misorientations around dislocations and measure them?
Author: Yes. It is possible as it can be observed in the case of the third sample Q3; but generally, the dislocations are grouped in bundles, and it is very difficult to measure the exact misorientations. Nevertheless, it is possible.

F. Hasselbach: You have studied different types of resonators using the "stroboscopic technique" and observed effects concerning the bulk acoustic waves and their interactions with the lattice defects. Is it possible to observe such interactions in resonators and transducers also for surface acoustic waves?
Author: Yes. This was done first by H. Graeff and his collaborators [4], and presently, we are doing such studies on Niobate lithium crystals.

F. Hasselbach: You stated that "the simulation of topographs" will be necessary to explain the observed "contrast". Is this always true? And, if not, in what cases is it necessary?
Author: It is true that the observation of a topograph generally permits one to understand some usual contrasts such as those given by the dislocations or the growth bands. In many other cases, the contribution of a theoretical explanation and also the simulation allow a better understanding of the contrast and the associated deformation given by a defect.